

Progressive Polytypism and Bandgap Tuning in Azetidinium Lead Halide Perovskites

Jiyu Tian^{1,2}, David B. Cordes¹, Alexandra M. Z. Slawin¹, Eli Zysman-Colman^{2,*} and Finlay D. Morrison^{1,*}

¹*EaStCHEM School of Chemistry, University of St Andrews, St Andrews, Fife, KY16 9ST, United Kingdom.*

²*Organic Semiconductor Centre, EaStCHEM School of Chemistry, University of St Andrews, St Andrews, Fife, KY16 9ST, United Kingdom.*

Abstract

Mixed halide azetidinium lead perovskites $\text{AzPbBr}_{3-x}\text{X}_x$ ($\text{X} = \text{Cl}$ or I) were obtained by mechanosynthesis. With varying halide composition from Cl^- to Br^- to I^- ; the chloride and bromide analogs both form in the hexagonal 6H polytype while the iodide adopts the 9R polytype. An intermediate 4H polytype is observed for mixed Br/I compositions. Overall, the structure progresses from 6H to 4H to 9R perovskite polytype with varying halide composition. Rietveld refinement of the powder X-ray diffraction patterns revealed a linear variation in unit cell volume as a function of the average radius of the anion, which is not only observed within the solid solution of each polytype (according to Vegard's law) but extends uniformly across all three polytypes. This is correlated with a progressive (linear) tuning of the bandgap from 3.43 to 2.00 eV. Regardless of halide, the family of azetidinium halide perovskite polytypes are highly stable, with no discernible change in properties over more than 6 months under ambient conditions.

Introduction

Hybrid organic inorganic halide perovskites have created much excitement as promising materials for solar cells,^{1–3} light-emitting diodes,^{4,5} and photodetectors,⁶ and backlit liquid crystal displays.⁷ These perovskite materials share a general formula AMX_3 , where the A-site cations occupy the interspace between MX_6 octahedra (M being a heavy group 14 element). The compositional variations among A, M and X result in a diverse range of structures with distinct chemical, physical and optoelectronic properties, including band structure,⁸ primarily due to variations in M-X bonding interactions and connectivity of octahedra. The most common polytype of these perovskites is the (pseudo-) cubic perovskite formed from a cubic (*c*-) close-packed stacking sequence of AX_3 layers and, as a result, corner-sharing MX_6 octahedra. In Ramsdell notation^{9,10} perovskites formed from entirely cubic close-packed AX_3 layers are indicated by the label 3C, representing the three close packing layers of the aristotype cell and C for the (pseudo-)cubic lattice type. For lead halide perovskites, such 3C polytypes are favored for tolerance factors, $0.83 < t \leq 1$,¹¹ which arise for relatively small A-site cations such as Cs^+ or methylammonium. For larger A-site cations, and $t > 1$, hexagonal polytypes are obtained.¹² These polytypes contain sequences of both cubic (*c*-) and hexagonal (*h*-) close-packed AX_3 layers, or only hexagonal (*h*-) packing. The resulting polytypes are also readily described using Ramsdell notation such as 2H (*hh...*), 4H (*hchc...*), 6H (*hcchcc...*) etc, where, again, the numerical value describes the number of packing layers in the unit cell and H describes the lattice type, which is hexagonal in this instance (although rhombohedral variants such as 9R also exist). These sequences generate a number of possible combinations of corner-sharing and face-sharing octahedra. In general, the bandgap of perovskite materials can be tuned by modifying the ratio of corner-sharing to face-sharing^{13,14} octahedra as the nature of octahedral connectivity affects the M-X orbital interactions that determine the energies of the valence and conduction bands.

Varying the halide composition is a common strategy for tuning the bandgap in hybrid halide perovskites.^{15–17} Nakamura *et al.*¹⁵ showed that the bandgap of 3C perovskite MAPbBr_{3-x} (MA = methylammonium) varied quadratically from 1.65 to 2.38 eV with increasing Br content accompanied by a symmetry change from tetragonal to cubic. Gratia *et al.*¹⁷ reported a crystallization process with a progressive structural change from 2H, 4H and 6H to 3C depending on x in $(\text{FAPbI}_3)_x(\text{MAPbBr}_3)_{1-x}$ (FA = formamidinium) and the annealing time of the perovskite

thin films; however, hexagonal polytypes were observed as phase mixtures in those compositions. Other benefits of mixed halide perovskites include improving solar cell power conversion efficiency^{18,19} and the stability of the perovskite materials.^{20,21} For example, Jeon *et al.* reported that incorporating 15% Br in FAPbI₃ lead to optimum power conversion efficiency of solar cells.¹⁸ Furthermore, Jun *et al.* reported that mixing 15-20% Br in MAPbI₃ resulted in solar cells that could keep 95% efficiency for more than 15 days after exposure to humidity, while the efficiency of MAPbI₃ cells dropped below 50% after the exposure.²⁰

One of the most commonly studied organic cations used at the A-site of this class of perovskites is methylammonium (MA⁺). MA-containing perovskite materials are often used as a reference point for studies of the optoelectronic properties of hybrid perovskites. However, poor resistance to moisture remains an obstacle to the commercialization of MA-containing perovskites, especially for MAPbI₃, which decomposes to PbI₂ in the presence of water.^{22,23} Other cations have been investigated to address the poor stability, such as formamidinium,^{24,25} Cs⁺^{26,27} azetidinium²⁸ and guanidinium²⁹, amongst others.

Mechanosynthesis has been reported as a simple and effective way to obtain organic-inorganic hybrid perovskites (OIHPs).^{16,30–32} In addition, grinding is an environmentally friendly (solvent free) approach that permits mass production and can reduce the particle size of the samples by mechanical force.³³ Many studies have shown that electrically powered ball milling is sufficient to synthesize single phase perovskite.^{30,31} Hong *et al.*³⁴ reported a successful solvent-free large scale mechanosynthesis of around 250 g of CsSnX₃ (X = I, Br or Cl) and FAPbI₃. By contrast, it has been reported that when using solution precipitation, the stoichiometry of precipitation products does not always match that of the reaction solution.^{35–37} This does not occur in mechanosynthesis. Thus, the latter method is used to synthesize mixed A-cation,^{31,32} mixed metal³⁸ and mixed halide perovskites¹⁶ with a more carefully controlled composition. Chen *et al.*¹⁶ reported a mechanosynthesis of mixed halide perovskite APbX₃ (A = MA and FA, X = Cl, Br and I), which yielded full-spectral emissions with a photoluminescence quantum yield of up to 92 %. Both mechano- and precipitation synthesis methods can be used to obtain pure phase OIHPs and have no obvious impact on the stability of compounds.³⁹

Azetidinium (Az⁺) is a four-membered ring ammonium (CH₂)₃NH₃⁺, which is calculated to be a possible candidate for organic-inorganic hybrid perovskite with a tolerance factor ranging from

0.98 to 1.02 (from AzPbI_3 to AzPbCl_3 perovskite).^{40,41} The preparation of both AzPbBr_3^{13} and AzPbI_3^{42} from solution have been reported, where 6H and 9R perovskites were obtained, respectively. Our previous study on AzPbBr_3^{13} showed that the material remains stable in ambient air for over 6 months. AzPbI_3 crystals were able to partially maintain the 9R crystalline state after being submerged in distilled water for 50 days⁴² and an AzPbI_3 thin film was reported to withstand exposure to moisture without decomposing²⁸, although the exposure time was only for a few seconds.

In the current study, a family of azetidinium mixed halide perovskites, $\text{AzPbBr}_{3-x}\text{X}_x$ ($\text{X} = \text{Cl}$ or I) were prepared by mechanosynthesis and their structures and optical absorption analyzed by both powder and single-crystal X-ray diffraction and absorption spectra, respectively. Besides the 6H polytype reported previously for AzPbBr_3^{13} and 9R polytype reported for AzPbI_3^{42} the chloride analogue is shown to also adopt the 6H structure and an intermediate hexagonal 4H polytype is identified for mixed Br-I compositions. All three polytypes can also be obtained by solution precipitation synthesis. Overall, the structure progresses from 6H to 4H to 9R perovskite polytypes with varying halide composition and with various degrees of solid solution formation within each structure type. The structural progression corresponds to a change in ratio of corner-sharing to face-sharing octahedra (Supporting Information, Table S1). Despite this variation in octahedral connectivity, the unit cell volume (normalized per formula unit) as a function of anion average radius varies linearly not only within each solid solution (in accordance with Vegard's law), but also across the entire polytype range. A tuneable bandgap is achieved ranging from 2.00 to 3.43 eV, which varies linearly as a function of average anion radius and the variation factor is similar to the reported factor of $\text{APbBr}_{3-x}\text{X}_x$ ($\text{A} = \text{MA}$, or FA , $\text{X} = \text{Cl}$ or I).⁴³⁻⁴⁵ The azetidinium halide perovskite polytypes remain highly stable for at least 6 months when stored in the ambient air.

Experimental Methods

Synthesis

PbBr_2 (98%), PbI_2 (98%) and hydroiodic acid in water (57%) were purchased from Alfa Aesar. Hydrobromic acid in water (48%) and AzCl (95%) were purchased from Fluorochem. All other reagents and solvents were obtained from commercial sources and used as received.

For preparation of azetidinium iodide (AzI), potassium hydroxide (1.30 g, 23 mmol, 1.5 equiv.) was dissolved in 3 mL DI water and mixed with azetidinium chloride (1.45 g, 15 mmol, 1 equiv.) under stirring for 30 min. The intermediate azetidine was extracted at 80 °C under reduced pressure and condensed with liquid nitrogen. Hydroiodic acid (3 mL, 23 mmol, 1.5 equiv.) was then added into the condensed azetidine solution and stirred for 30 min at room temperature. The solvent was then removed under reduced pressure at 80 °C. The crude products were dissolved in 3 mL EtOH and the product recrystallized from diethyl ether. The recovered solid was dried under vacuum for 24 h before use. White needle-like crystals were obtained. The NMR of AzI is shown in Figure S1. Yield: 86%. Mp.: 137–138 °C. ¹H NMR (500 MHz, DMSO-*d*₆) δ (ppm) 8.42 (s, 2H), 3.98 – 3.89 (m, 4H), 2.37 (p, *J* = 8.3 Hz, 2H). ¹³C NMR (126 MHz, DMSO-*d*₆) δ (ppm) 46.53, 18.93. Elemental Analysis. Calculated for C₃H₈NI: C, 19.48; H, 4.36; N, 7.57; I, 68.59; Found: C, 19.61; H, 4.24; N, 7.66.

AzPbCl₃ samples were prepared by dissolving AzCl and PbCl₂ (1:1) in DMSO (2 mL, 0.4 M) at room temperature and in air. After stirring for 1 h clear solutions were obtained. DCM (8 mL) was added slowly into the solution and the vial was shaken for 1 min and then left to stand for 10 min before vacuum filtration. The resulting powders were washed with 10 mL DCM twice and dried under vacuum for 24 h. The samples were white powders. Precipitation synthesis attempts of AzPbBr_{1.5}I_{1.5} and AzPbI₃ samples were carried out by mixing appropriate molar ratios AzI, PbBr₂ and PbI₂ or AzI and PbI₂ in DMF (0.15 M) or DMF/γ-butyrolactone (1:1, 0.05M) at room temperature. Sonication and stirring were applied to aid in dissolving the raw materials. DCM (20 mL) was added slowly into the solution and the vial was shaken for 1 min and then left to stand for 2 min before vacuum filtration. The resulting powders were washed with 10 mL DCM twice and dried under vacuum for 24 h.

Preparation of both AzPbCl_xBr_{3-x} and AzPbI_xBr_{3-x} solid solutions with 0 ≤ *x* ≤ 3 was carried out by mechanosynthesis. Appropriate molar ratios of Az/halide source (AzPbCl₃, AzBr or AzI) and lead/halide source (PbCl₂, PbBr₂ or PbI₂) were ground together in a Fritsch Pulverisette planetary ball mill at 600 rpm for 1 hour using 60 cm³ Teflon pots and high-wear-resistant zirconia media (nine zirconia grinding media 10 mm diameter spheres).

Single crystals of AzPbCl₃, AzPbBr_{1.5}I_{1.5} and AzPbI₃ for comparison with mechanosynthesized samples were prepared by slow diffusion of antisolvent DCM/acetonitrile/acetonitrile into DMSO,

DMF/DSMO (4:1) and DMF/ γ -butyrolactone (1:1) solution, respectively. AzPbCl₃ appears as white needle-like crystals while AzPbBr_{1.5}I_{1.5} and AzPbI₃ crystals are bright yellow and dark red, respectively. During crystallization of AzPbBr_{1.5}I_{1.5}, there was evidence of formation of crystals of other compounds; in one case indexing of the data suggested the presence of AzPbI₃. This suggests that the mixed halide is not favored against the single-halide forms of the complex during recrystallization and vice versa. Given some of the data-issues encountered (*vide infra*), it is possible that the selected crystals of AzPbBr_{1.5}I_{1.5} may have contained domains or crystallites of AzPbBr₃ or AzPbI₃.

Single crystal samples prepared by precipitation synthesis and powder samples prepared by either precipitation or mechanosynthesis routes were characterized by single crystal and powder X-ray diffraction (SCXRD and PXRD, respectively). SCXRD data were collected at either at 293, 173, or 93 K using a Rigaku FR-X Ultrahigh Brilliance Microfocus RA generator/confocal optics with XtaLAB P200 diffractometer [Mo K α radiation ($\lambda = 0.71075 \text{ \AA}$)]. Intensity data were collected using ω -steps accumulating area detector images spanning at least a hemisphere of reciprocal space. Details of structure solution and refinement are provided in the Supporting Information. PXRD was carried out either using a PANalytical Empyrean diffractometer with Cu K $\alpha 1$ ($\lambda = 1.5406 \text{ \AA}$). Rietveld refinements of PXRD data using GSAS⁴⁶ were used to confirm phase formation and for determination of lattice parameters.

Optical properties were determined from solid-state absorption spectra recorded using a JASCO-V650 double beam spectrophotometer and bandgaps were calculated using the ‘Band-Gap Calculation’ program of the spectrophotometer which applies the Tauc method.

Sample morphologies were investigated using a Jeol JSM-5600 Scanning Electron Microscope with an accelerating voltage set at 5 kV.

¹H and ¹³C Nuclear magnetic resonance (NMR) spectra were recorded on a Bruker Advance spectrometer (500 MHz for ¹H, 126 MHz for ¹³C). ¹H and ¹³C NMR spectra were referenced to residual solvent peaks with respect to TMS ($\delta = 0 \text{ ppm}$).

Melting points of the perovskite were measured in a capillary using an Electrothermal MEL-TMP 1101D melting point apparatus.

Results and Discussion

Commercially available AzCl was found to be too impure (< 90%, discussed in Supporting Information and shown in Figure S2) to use in the mechanosynthesis, so AzPbCl₃ prepared by precipitation synthesis, with purity confirmed by powder X-ray diffraction (PXRD), was used as the Az/Cl source. Attempts to prepare AzPbCl₃ by mechanosynthesis using commercial AzCl required a stoichiometric excess of AzCl to converge to the desired product. While PXRD showed successful preparation of single-phase AzPbCl₃ using this excess (Figure S3), the presence of small amounts of AzCl, which may not be detectable by PXRD, cannot be excluded. Thus, the following analysis of AzPbCl₃ was based only on precipitation-synthesized samples.

The color progression (Figure 1a) of the as-synthesized AzPbCl_xBr_{3-x} is subtle and ranges from white (AzPbCl₃) to pale yellow (AzPbBr₃); the colors of the AzPbBr_xI_{3-x} series, by contrast, show a clear and systematic change from pale yellow (AzPbBr₃) to red orange (AzPbI₃). The PXRD of the mixed halide perovskites are shown in Figures 1b and 1c. The PXRD of AzPbCl₃ shows the same 6H hexagonal structure as AzPbBr₃.¹³ Single crystal X-ray diffraction (SCXRD) at ambient temperature and 173 K confirms the 6H polytype (Figure 2) with space group *P*6₃/*mmc* [PXRD (ambient): $a = 8.515(6)$ Å, $c = 20.44(9)$; SCXRD (293 K): $a = 8.5166(2)$ Å, $c = 20.4424(6)$ Å; SCXRD (173 K): $a = 8.4763(2)$ Å, $c = 20.3303(6)$ Å]. The PXRD data of the Br-rich region for AzPbBr_{3-x}Cl_x samples show additional broad features in the base of the main peaks and which are especially evident around 12 – 14°. These features match well with the reported features from bimodal CdS particles⁴⁷ and indicate the presence of multiple subpopulations of different sizes of 6H perovskite particles. In our previous study, the PXRD of precipitation-synthesized AzPbBr₃ did not show such features.¹³ Scanning electron microscopy (SEM) of both mechano- and precipitation synthesized AzPbBr₃ (Figure S4) indicate the presence of a large proportion of relatively smaller particles in the mechanothesized AzPbBr₃, explaining the broad base of the PXRD peaks in Figure 1b.

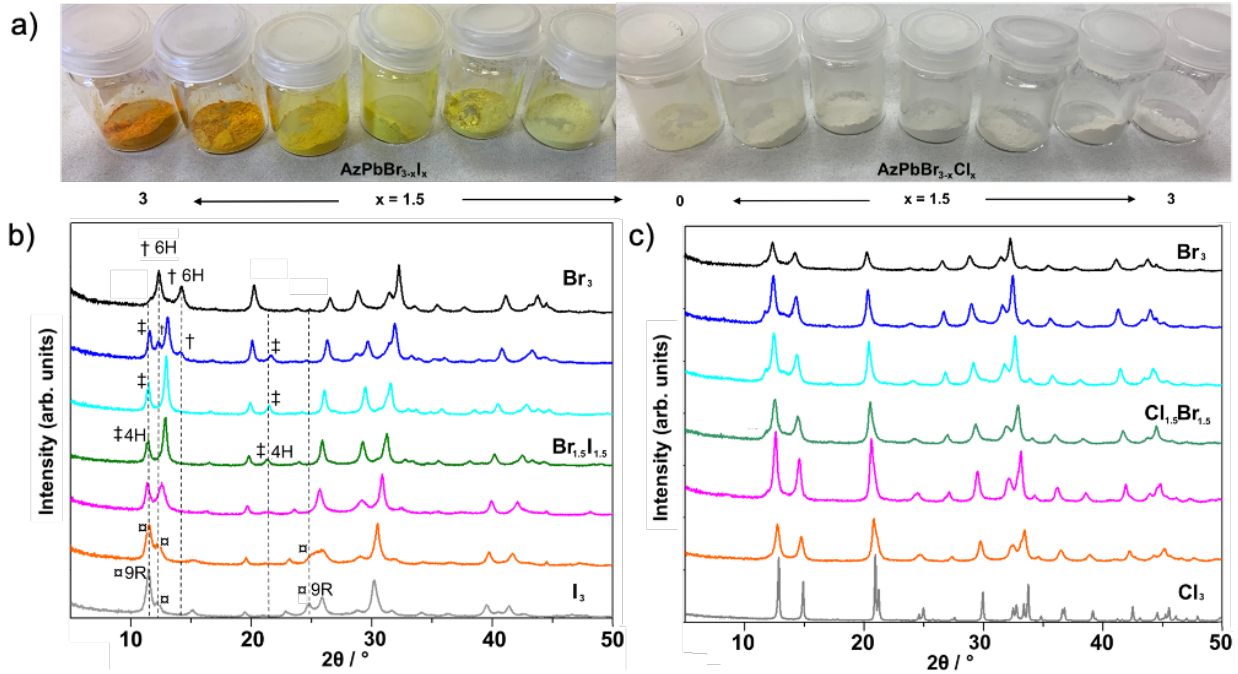


Figure 1. (a) Photos and (b, c) PXRD patterns of mixed halide perovskite: $\text{AzPbBr}_{3-x}\text{X}_x$ ($\text{X} = \text{Cl}$ or I) with composition $0 \leq x \leq 3$ (in $x = 0.5$ increments) prepared by mechanosynthesis, except AzPbCl_3 which was prepared by precipitation synthesis. $\ddagger\text{6H}$, $\ddagger\text{4H}$, $\square\text{9R}$ indicate selected peaks for each corresponding polytype.

AzPbI_3 has been reported previously as a 9R polytype⁴² and Rietveld refinement (Figure S5) of PXRD data confirms that the 9R AzPbI_3 perovskite can also be obtained easily by mechanosynthesis compared with the reported two-step recrystallisation method in solution.⁴² This is also confirmed by the SCXRD structure, although, as has been the case in previous attempts to determine the structure of AzPbI_3 by SCXRD,⁴² the apparent crystal quality prevented the confirmation of the Az^+ cation sites. This was observed for data collected at both ambient temperature and 173 K. In the case of this structure, both resulted in a lattice parameter, a , smaller than that determined by Rietveld refinement, the ambient temperature structure being closer to that seen in the refined PXRD data, however, both SCXRD structures had a c lattice parameter larger than that determined by Rietveld refinement [SCXRD (293 K): $a = 9.0835(5)$ Å, $c = 35.104(3)$ Å; SCXRD (173 K): $a = 8.983(2)$ Å, $c = 35.130(10)$ Å; PXRD (ambient) $a = 9.101(1)$ Å, $c = 35.00(2)$ Å]. The PXRD data of $\text{AzPbBr}_x\text{I}_{3-x}$ ($x \leq 2$) seem to indicate a structure that was neither 6H, 9R nor a two-phase mixture of these two polytypes; however, the hypothesis was that $\text{AzPbBr}_x\text{I}_{3-x}$ ($x \leq 2$)

is still some form of perovskite (or a mixture of perovskite polytypes). Analysis of the PXRD data of $\text{AzPbBr}_{1.5}\text{I}_{1.5}$, in particular, the d -spacing of the two major peaks at 11.41° and 12.86° , reveals the intermediate structure to be the 4H polytype with $P6_3/mmc$ space group (Figure 2). The 4H perovskite structure has an $(hc)_2$ stacking sequence in Jagodzinski notation, resulting in alternating face-sharing and corner-sharing octahedra. The goodness-of-fit parameters from the Rietveld refinement of $\text{AzPbBr}_{1.5}\text{I}_{1.5}$ to an adapted 4H model (Figure S6) indicate a good fit: $\chi^2 = 3.509$, $wR_p = 7.5\%$. SCXRD of the $\text{AzPbBr}_{1.5}\text{I}_{1.5}$ single crystals prepared by precipitation suggested that a mixture of phases exist, potentially including the AzPbX_3 single-halide material; no evidence of mixed phase was evident in the same compositions prepared by mechanochemical synthesis, again highlighting the need for caution for samples prepared using the kinetically-controlled precipitation route compared to thermodynamically-controlled mechanochemical synthesis.³¹ However, it did prove possible to isolate and structurally characterize $\text{AzPbBr}_{1.5}\text{I}_{1.5}$ by SCXRD. As was the case with the iodide compound, crystal quality precluded modelling of the Az^+ sites, both for ambient temperature data, and for that collected at 173 K. Both structures showed lattice parameters smaller than that determined by Rietveld refinement (Table S2), the ambient temperature structure being closer to that seen in the refined PXRD data [SCXRD (293 K): $a = 8.958(4)$ Å, $c = 14.846(6)$ Å; SCXRD (93 K): $a = 8.851(5)$ Å, $c = 14.760(8)$ Å; PXRD (ambient): $a = 8.964(3)$ Å, $c = 14.82(9)$ Å]. The PXRD of the samples from the antisolvent precipitation synthesis of 4H($\text{AzPbBr}_{1.5}\text{I}_{1.5}$) and 9R(AzPbI_3) indicate that it is possible to obtain the corresponding phase with antisolvent precipitation (Figure S7).

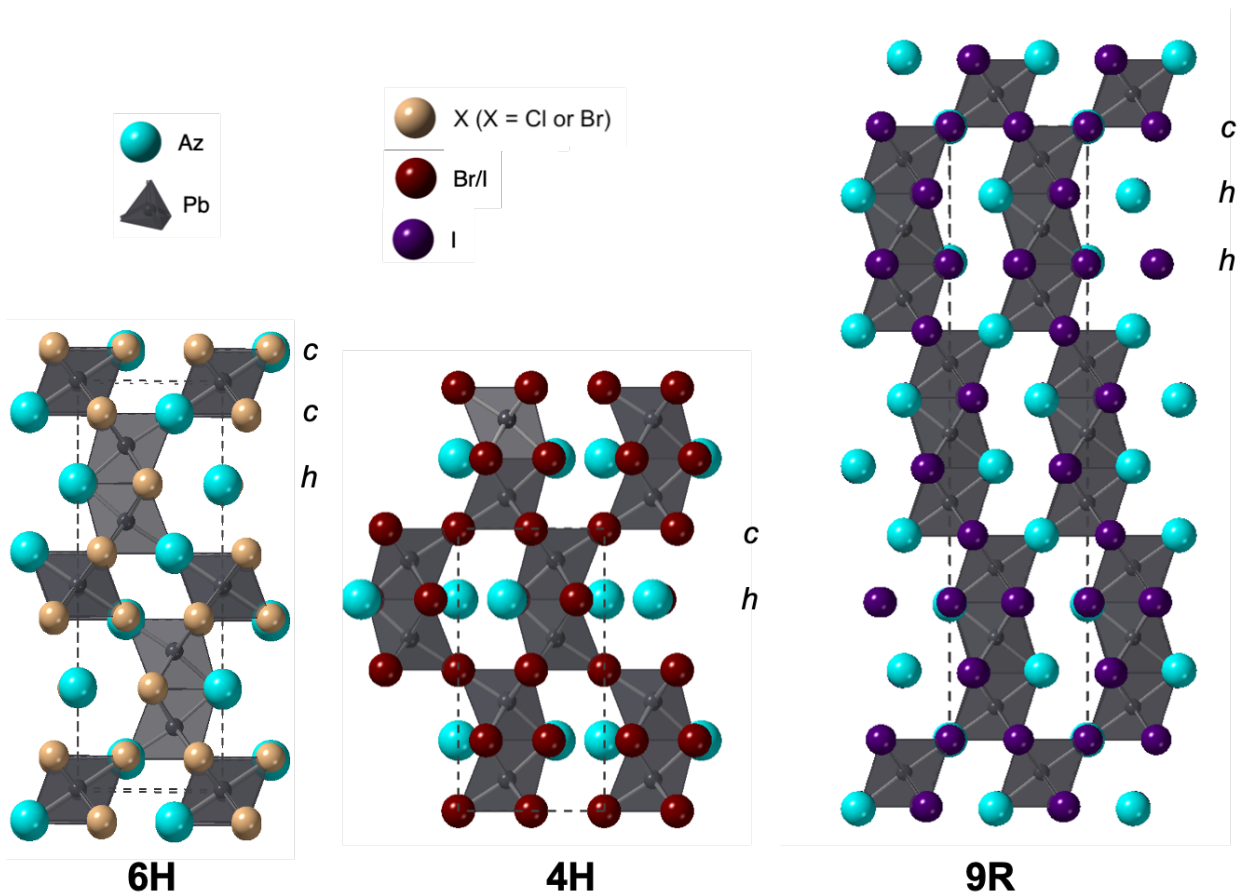


Figure 2. Structures determined from (both powder and single crystal) XRD data of different azetidinium lead halide perovskite polytypes: 6H (AzPbX_3 , $\text{X} = \text{Br}, \text{Cl}$), 4H ($\text{AzPbBr}_{1.5}\text{I}_{1.5}$) and 9R (AzPbI_3) viewed along a , where the AX_3 stacking sequence is denoted with h - and c - for hexagonal and cubic close packed layers, respectively.

The mechanosynthesized perovskite samples were re-examined by PXRD after being stored in ambient air for 6 months and no visual or structural decomposition was observed (Figure S8). The thermal stability of the Az mixed halide perovskite was tested by heating the mechanosynthesized powder samples to 100 °C (a commonly used annealing temperature^{6,48}) for 2 or 15 hours. These heated samples were reanalyzed by PXRD, and the results are shown in Figure S9. The single halide perovskites AzPbX_3 ($\text{X} = \text{Cl}, \text{Br}, \text{I}$) showed excellent thermal stability with no decomposition observed after 15 hours of heating at 100 °C. For the mixed halide 4H $\text{AzPbBr}_{1.5}\text{I}_{1.5}$ sample, however, weak additional peaks were observed suggesting the onset of partial

decomposition after 15 hours of heating. Such decomposition was not found in the samples after 2 hours of heating at 100 °C. These observations agree with the melting point tests which show that the melting points of the mixed halide compositions are lower than the single halide phases. The melting point of $\text{AzPbBr}_{1.5}\text{I}_{1.5}$ is 190-192°C, while the melting points of single halide perovskite AzPbX_3 ($\text{X} = \text{Cl}, \text{Br}, \text{I}$) are 219-220 °C, 233-234 °C and 228-232 °C, respectively. This suggests that Az mixed halide perovskites are less resistant to thermal decomposition compared to the single halide perovskites.

To study the solid solutions within, and transition between, these polytypes, the lattice parameters of each mechanosynthesized composition were determined by Rietveld refinement of PXRD data. The lattice parameters of the single halide perovskites AzPbX_3 ($\text{X} = \text{Cl}, \text{Br}, \text{I}$) and also 4H- $\text{AzPbBr}_{1.5}\text{I}_{1.5}$ are shown in Table 1. The average interlayer distance along the c -axis (\bar{c}) and lattice parameter a increase with the transition sequence from 6H to 4H to 9R. The cell volume (normalized to the number of formula units per unit cell) of those polytypes varies linearly as a function of average anion radius, Figure 3a (the average anion radius was calculated using $r_{\text{I}} = 220$ pm, $r_{\text{Br}} = 196$ pm and $r_{\text{Cl}} = 181$ pm according to Shannon⁴¹). While this linear variation within each polytype solid solution is expected in accordance with Vegard's law, it is interesting to note that the linear relationship extends continuously across all three polytypes. Presumably this reflects the AX_3 close packing volume; however, it suggests that the polytype adopted is largely driven by the degree of Pb-Pb interactions, which is emphasized in face-sharing (h) layers. The substitution of increasingly large, and less electronegative, halide anions result in an expansion of MX_6 octahedra, which decreases the electrostatic (Madelung) energy of the ionic crystals and allows for more face sharing octahedral layers and Pb-Pb proximity.

Table 1. Lattice parameters and goodness-of-fit parameters for Rietveld refinement of PXRD data for single and mixed halide perovskite compositions.

	AzPbCl ₃	AzPbBr ₃	AzPbBr _{1.5} I _{1.5}	AzPbI ₃
Space group	<i>P</i> 6 ₃ / <i>mmc</i>	<i>P</i> 6 ₃ / <i>mmc</i>	<i>P</i> 6 ₃ / <i>mmc</i>	<i>R</i> ̄3
Polytype	6H	6H	4H	9R
<i>a</i> / Å	8.515(6)	8.758(2)	8.964(3)	9.101(1)
<i>c</i> / Å	20.44(9)	21.42(5)	14.82(9)	35.00(2)
volume / Å ³	1284.2(6)	1423.3(0)	1032.0(4)	2510.8(3)
<i>c</i> ̄ / Å *	3.408	3.570	3.707	3.889
χ^2	3.066	4.697	3.509	1.545
w <i>R</i> _p	0.069	0.083	0.075	0.056

* The average interlayer distance along *c*-axis.

In addition to the 4H, 6H and 9R single phase solid solutions, intermediate two-phase regions of 6H-4H and 4H-9R were also identified by PXRD, as shown in Figure 3a. For the 6H-4H two phase-region, the peaks of both phases could be readily identified, but the boundary of the 4H-9R two-phase region was difficult to ascertain due to the overlap of the major peaks (Figure 1b). Attempts at two-phase refinement of PXRD data of both two-phase regions were unsuccessful due to the overall breadth of peaks, overlap of major peaks and relatively low intensities of non-overlapping peaks. As a result, no lattice parameters are provided for the 6H-4H two-phase region. For the 4H-9R two-phase region, the data for compositions AzPbBrI₂ and AzPbBr_{0.6}I_{2.4} which appear close to the phase boundaries were refined as single-phase 4H and 9R, respectively, as approximations, and the resulting lattice parameters matched quite well with the linear fit as a function of average anion radius. As a general comparison, the cell volumes as a function of average anion radius for 3C FAPbX₃ and MAPbX₃ mixed halide perovskites⁴³⁻⁴⁵ are shown in

Figure S10a and display similar linear behavior, but this unlike the AzPbX_3 compositions of the current study all MA- and FA-compositions adopt a single (3C) polytype.

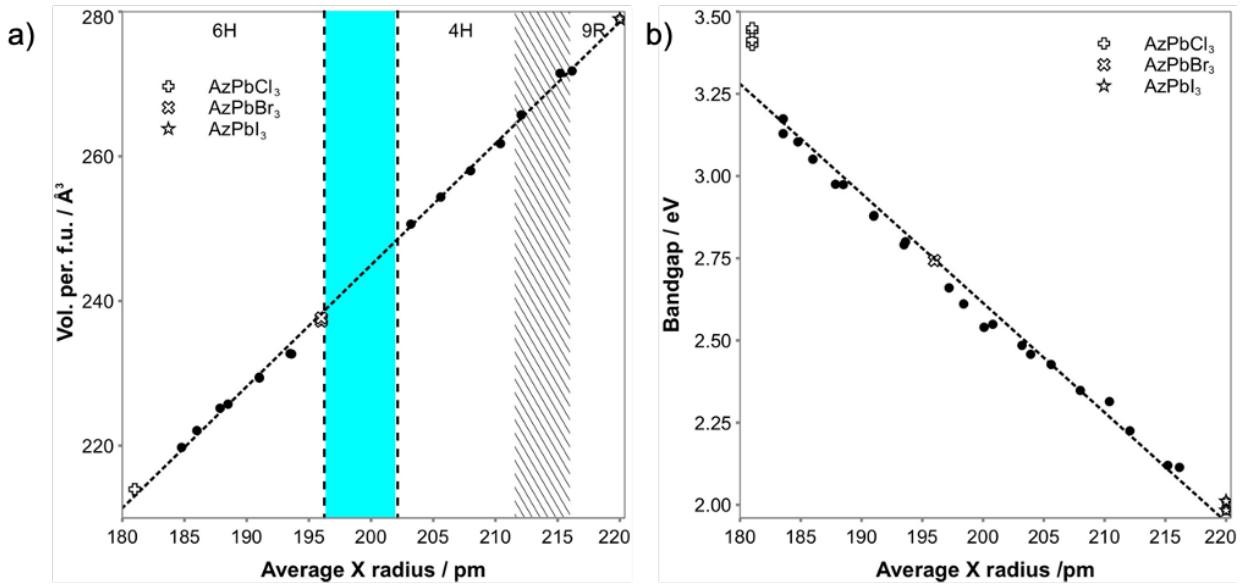


Figure 3. a) Cell volume (per formula unit) of mixed halide perovskite determined by Rietveld refinement of PXRD data and b) the bandgap determined from absorption spectra of samples $\text{AzPbBr}_{3-x}\text{X}_x$ ($\text{X} = \text{Cl}$ or I) with composition $0 \leq x \leq 3$ plotted as a function of average halide anion radius. Intermediate 6H-4H (shaded) and 4H-9R (hatched) two phase-regions are indicated.

The optical properties of the different phases were studied by absorption spectroscopy (Figure 4). The absorption onsets are systematically red-shifted with increasing average anion size (from Cl to I). The absorption onset of $\text{AzPbBr}_{3-x}\text{X}_x$ ($\text{X} = \text{Cl}$ or I , $0 \leq x \leq 3$) samples show a red shift from *ca.* 360 nm (3.44 eV, AzPbCl_3), to *ca.* 450 nm (2.76 eV, AzPbBr_3), to *ca.* 615 nm (2.02 eV, AzPbI_3). The background absorption of intermediate compositions in $\text{AzPbCl}_x\text{Br}_{3-x}$ samples lies above the normalized zero baseline, especially for $x = 2.5$. This might result from a small number of Br-rich crystallites on the sample surface, the amount of which is too small to be detected in PXRD. The absorption of AzPbI_3 bore close resemblance to the reported spectrum,⁴² where three well-defined transitions could be detected; the peak maxima of the three well-defined transitions are at 551, 506, 470 nm while the reported transitions peak at 554, 503, 462 nm.

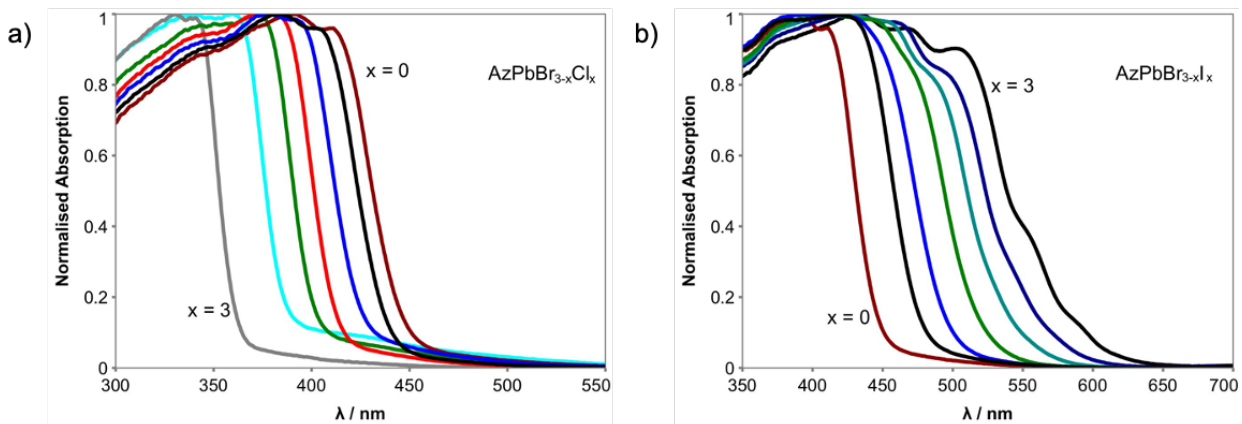


Figure 4. Absorption spectra of a) $\text{AzPbBr}_{3-x}\text{Cl}_x$ b) $\text{AzPbBr}_{3-x}\text{I}_x$ ($0 \leq x \leq 3$, in $x = 0.5$ increments); all samples were prepared by mechanosynthesis.

The bandgap as a function of halide composition for the mixed halide perovskites is shown in Figure 3b. The bandgap of AzPbCl_3 and AzPbI_3 were calculated to be 3.43 ± 0.02 eV and 2.00 ± 0.02 eV, respectively. The latter is in good agreement with the previously reported value of 1.97 eV.⁴² The bandgap varies linearly as a function of average anion radius, despite the change of halide composition and octahedral connectivity. As discussed in our previous study, the varying ratio of corner-sharing to face-sharing octahedral connectivity changes the efficiency of Pb-X orbital overlap; in conjunction with the change in Pb-X bond length, average bond angles and covalency which give rise to the bandgap variation.¹³ Comparison of the behavior of the Az-based perovskites with corresponding MA-, and FA-based mixed halide perovskites shows that the lattice parameter progression as a function of halide composition is linear in all cases; however, the reported relation of bandgap versus halide composition is not consistent across these studies. Some studies reported a nonlinear relation, which is described as a bowing effect,^{20,43,49} while other studies document a linear progression^{50,51} as observed here. Bandgap “bowing” is often fitted to a second order polynomial, with a bowing parameter b as the binominal coefficient of the fitting equation. The bowing parameters of $\text{MAPbBr}_{3-x}\text{X}_x$ ($\text{X} = \text{Cl}$ or I) are relatively small (7×10^{-4} to 0.33)^{20,43} compared to the bowing parameters (0.5 to 1.33) found for other mixed metal perovskite systems.^{52–55} Our study illustrates a good example of a linear variation between bandgap and halide composition, and it is as of yet unclear why both linear and non-linear relationship were reported

for other mixed halide perovskites with same organic cation and metal. However, this may relate to anion segregation when prepared using kinetically-controlled precipitation routes.^{31,56}

Summary and Conclusions

Following on from studies on azetidinium lead bromide, mixed halide compositions, $\text{AzPbBr}_{3-x}\text{X}_x$ ($\text{X} = \text{Cl}$ or I), were successfully synthesized using a mechanosynthetic grinding method. The single-phase single halide materials AzPbX_3 ($\text{X} = \text{Cl}$, Br or I) were shown to be stable in air for $>$ six months and no decomposition was observed after 15 hours of heating at 100 °C. In addition to the 6H polytype reported previously for AzPbBr_3 ,¹³ and 9R polytype reported for AzPbI_3 ,⁴² AzPbCl_3 was also shown to form in the 6H polytype and an additional 4H polytype was found for $\text{AzPbBr}_{3-x}\text{I}_x$ (*ca.* $0 < x \leq 2$) compositions. With varying halide composition, the structure progresses from 6H to 4H to 9R perovskite polytype. A complete (continuous) solid solution is formed for compositions with the 6H structure and partial solid solutions form between the 6H and 4H and 4H and 9R polytypes. A linear variation in unit cell volume (scaled per formula unit) as a function of anion average radius is observed not only within the solid solution of each polytype (according to Vegard's law) but continuously across all three polytypes, which, to the best of our knowledge, is the first time that Vegard's law-type behavior has been observed across several polytypes. This linear relationship extending across all compositions is accompanied by a linearly tuneable bandgap ranging from 2.00 to 3.43 eV as a function of average anion radius without any observations of a "bowing effect". The linear variation of bandgap across all AzPbX_3 compositions (and polytypes) is comparable to that observed in $\text{APbBr}_{3-x}\text{X}_x$ ($\text{A} = \text{MA}$, or FA , $\text{X} = \text{Cl}$ or I) but which all adopt a single (3C) polytype.^{43–45}

Associated content

Supporting Information

The Supporting Information contains additional experimental information including: details of ^1H NMR analysis, PXRD analysis, SCXRD analysis, SEM, examples of Rietveld refinement, details

of thermal stability, absorption spectra and bandgap analysis. The research data supporting this publication can be accessed at [].

Author information

Corresponding authors:

eli.zysman-colman@st-andrews.ac.uk

finlay.morrison@st-andrews.ac.uk

Acknowledgements

We thank the Chinese Scholarship Council for Ph.D. Studentship support (to JT, CSC No. 201603780020).

References

- (1) Hou, Y.; Aydin, E.; De Bastiani, M.; Xiao, C.; Isikgor, F. H.; Xue, D.-J.; Chen, B.; Chen, H.; Bahrami, B.; Chowdhury, A. H.; et al. Efficient Tandem Solar Cells with Solution-Processed Perovskite on Textured Crystalline Silicon. *Science* (80-.). **2020**, *367* (6482), 1135–1140.
- (2) Alsalloum, A. Y.; Turedi, B.; Zheng, X.; Mitra, S.; Zhumekenov, A. A.; Lee, K. J.; Maity, P.; Gereige, I.; AlSaggaf, A.; Roqan, I. S.; et al. Low-Temperature Crystallization Enables 21.9% Efficient Single-Crystal MAPbI₃ Inverted Perovskite Solar Cells. *ACS Energy Lett.* **2020**, *5* (2), 657–662.
- (3) Liu, J.; Han, Q.; Bai, Y.; Du, K. Z.; Li, T.; Ji, D.; Zhou, Y.; Cao, C.; Shin, D.; Ding, J.; et al. Additive Engineering for High-Performance Room-Temperature-Processed Perovskite Absorbers with Micron-Size Grains and Microsecond-Range Carrier Lifetimes. *Energy Environ. Sci.* **2017**, *10* (11), 2365–2371.
- (4) Liang, H.; Yuan, F.; Johnston, A.; Gao, C.; Choubisa, H.; Gao, Y.; Wang, Y.; Sagar, L. K.; Sun, B.; Li, P.; et al. High Color Purity Lead-Free Perovskite Light-Emitting Diodes via Sn

Stabilization. *Adv. Sci.* **2020**, *7* (8), 1903213.

- (5) Ma, D.; Todorović, P.; Meshkat, S.; Saidaminov, M. I.; Wang, Y.-K.; Chen, B.; Li, P.; Scheffel, B.; Quintero-Bermudez, R.; Fan, J. Z.; et al. Chloride Insertion–Immobilization Enables Bright, Narrowband, and Stable Blue-Emitting Perovskite Diodes. *J. Am. Chem. Soc.* **2020**, *142* (11), 5126–5134.
- (6) Cao, M.; Tian, J.; Cai, Z.; Peng, L.; Yang, L.; Wei, D. Perovskite Heterojunction Based on CH₃NH₃PbBr₃ Single Crystal for High-Sensitive Self-Powered Photodetector. *Appl. Phys. Lett.* **2016**, *109* (23), 233303.
- (7) Lin, J.; Lu, Y.; Li, X.; Huang, F.; Yang, C.; Liu, M.; Jiang, N.; Chen, D. Perovskite Quantum Dots Glasses Based Backlit Displays. *ACS Energy Lett.* **2021**, *6* (2), 519–528.
- (8) Stoumpos, C. C.; Malliakas, C. D.; Kanatzidis, M. G. Semiconducting Tin and Lead Iodide Perovskites with Organic Cations: Phase Transitions, High Mobilities, and near-Infrared Photoluminescent Properties. *Inorg. Chem.* **2013**, *52* (15), 9019–9038.
- (9) Stein, F.; Palm, M.; Sauthoff, G. Structure and Stability of Laves Phases. Part I. Critical Assessment of Factors Controlling Laves Phase Stability. *Intermetallics* **2004**, *12* (7–9), 713–720.
- (10) Patrick, L. Inequivalent Sites and Multiple Donor and Acceptor Levels in SiC Polytypes. *Phys. Rev.* **1962**, *127* (6), 1878–1880.
- (11) Bartel, C. J.; Sutton, C.; Goldsmith, B. R.; Ouyang, R.; Musgrave, C. B.; Ghiringhelli, L. M.; Scheffler, M. New Tolerance Factor to Predict the Stability of Perovskite Oxides and Halides. *Sci. Adv.* **2019**, *5* (2), eaav0693.
- (12) Kamminga, M. E.; Fang, H.-H.; Filip, M. R.; Giustino, F.; Baas, J.; Blake, G. R.; Loi, M. A.; Palstra, T. T. M. Confinement Effects in Low-Dimensional Lead Iodide Perovskite Hybrids. *Chem. Mater.* **2016**, *28* (13), 4554–4562.
- (13) Tian, J.; Cordes, D. B.; Quarti, C.; Beljonne, D.; Slawin, A. M. Z.; Zysman-Colman, E.; Morrison, F. D. Stable 6H Organic-Inorganic Hybrid Lead Perovskite and Competitive Formation of 6H and 3C Perovskite Structure with Mixed A Cations. *ACS Appl. Energy Mater.* **2019**, *2* (8), 5427–5437.

- (14) Stoumpos, C. C.; Mao, L.; Malliakas, C. D.; Kanatzidis, M. G. Structure-Band Gap Relationships in Hexagonal Polytypes and Low-Dimensional Structures of Hybrid Tin Iodide Perovskites. *Inorg. Chem.* **2017**, *56* (1), 56–73.
- (15) Nakamura, Y.; Shibayama, N.; Hori, A.; Matsushita, T.; Segawa, H.; Kondo, T. Crystal Systems and Lattice Parameters of CH₃NH₃Pb(I₁-XBr_x)₃ Determined Using Single Crystals: Validity of Vegard's Law. *Inorg. Chem.* **2020**, *59* (10), 6709–6716.
- (16) Chen, D.; Li, J.; Chen, X.; Chen, J.; Zhong, J. Grinding Synthesis of APbX₃ (A = MA, FA, Cs; X = Cl, Br, I) Perovskite Nanocrystals. *ACS Appl. Mater. Interfaces* **2019**, *11* (10), 10059–10067.
- (17) Gratia, P.; Zimmermann, I.; Schouwink, P.; Yum, J.-H.; Audinot, J.-N.; Sivula, K.; Wirtz, T.; Nazeeruddin, M. K. The Many Faces of Mixed Ion Perovskites: Unraveling and Understanding the Crystallization Process. *ACS Energy Lett.* **2017**, *2* (12), 2686–2693.
- (18) Jeon, N. J.; Noh, J. H.; Yang, W. S.; Kim, Y. C.; Ryu, S.; Seo, J.; Seok, S. Il. Compositional Engineering of Perovskite Materials for High-Performance Solar Cells. *Nature* **2015**, *517* (7535), 476–480.
- (19) Azam, M.; Yue, S.; Xu, R.; Liu, K.; Ren, K.; Sun, Y.; Liu, J.; Wang, Z.; Qu, S.; Lei, Y.; et al. Highly Efficient Solar Cells Based on Cl Incorporated Tri-Cation Perovskite Materials. *J. Mater. Chem. A* **2018**, *6* (28), 13725–13734.
- (20) Noh, J. H.; Im, S. H.; Heo, J. H.; Mandal, T. N.; Seok, S. Il. Chemical Management for Colorful, Efficient, and Stable Inorganic-Organic Hybrid Nanostructured Solar Cells. *Nano Lett.* **2013**, *13* (4), 1764–1769.
- (21) Yang, W. S.; Park, B.-W.; Jung, E. H.; Jeon, N. J.; Kim, Y. C.; Lee, D. U.; Shin, S. S.; Seo, J.; Kim, E. K.; Noh, J. H.; et al. Iodide Management in Formamidinium-Lead-Halide Based Perovskite Layers for Efficient Solar Cells. *Science (80-.).* **2017**, *356* (6345), 1376–1379.
- (22) Philippe, B.; Park, B. W.; Lindblad, R.; Oscarsson, J.; Ahmadi, S.; Johansson, E. M. J.; Rensmo, H. Chemical and Electronic Structure Characterization of Lead Halide Perovskites and Stability Behavior under Different Exposures-A Photoelectron Spectroscopy Investigation. *Chem. Mater.* **2015**, *27* (5), 1720–1731.

- (23) Ito, S. Research Update: Overview of Progress about Efficiency and Stability on Perovskite Solar Cells. *APL Mater.* **2016**, *4* (9), 091504.
- (24) Wang, Y.; Wu, T.; Barbaud, J.; Kong, W.; Cui, D.; Chen, H.; Yang, X.; Han, L. Stabilizing Heterostructures of Soft Perovskite Semiconductors. *Science* **2019**, *365* (6454), 687–691.
- (25) Xu, W.; Hu, Q.; Bai, S.; Bao, C.; Miao, Y.; Yuan, Z.; Borzda, T.; Barker, A. J.; Tyukalova, E.; Hu, Z.; et al. Rational Molecular Passivation for High-Performance Perovskite Light-Emitting Diodes. *Nat. Photonics* **2019**, *13* (6), 418–424.
- (26) Abdi-Jalebi, M.; Andaji-Garmaroudi, Z.; Cacovich, S.; Stavrakas, C.; Philippe, B.; Richter, J. M.; Alsari, M.; Booker, E. P.; Hutter, E. M.; Pearson, A. J.; et al. Maximizing and Stabilizing Luminescence from Halide Perovskites with Potassium Passivation. *Nature* **2018**, *555* (7697), 497–501.
- (27) Zheng, X.; Hou, Y.; Bao, C.; Yin, J.; Yuan, F.; Huang, Z.; Song, K.; Liu, J.; Troughton, J.; Gasparini, N.; et al. Managing Grains and Interfaces via Ligand Anchoring Enables 22.3%-Efficiency Inverted Perovskite Solar Cells. *Nat. Energy* **2020**, *5* (2), 131–140.
- (28) Pering, S. R.; Deng, W.; Troughton, J. R.; Kubiak, P. S.; Ghosh, D.; Niemann, R. G.; Brivio, F.; Jeffrey, F. E.; Walker, A. B.; Islam, M. S.; et al. Azetidinium Lead Iodide for Perovskite Solar Cells. *J. Mater. Chem. A* **2017**, *5* (39), 20658–20665.
- (29) Jodłowski, A. D.; Roldán-Carmona, C.; Grancini, G.; Salado, M.; Ralaiarisoa, M.; Ahmad, S.; Koch, N.; Camacho, L.; de Miguel, G.; Nazeeruddin, M. K. Large Guanidinium Cation Mixed with Methylammonium in Lead Iodide Perovskites for 19% Efficient Solar Cells. *Nat. Energy* **2017**, *2* (12), 972–979.
- (30) Protesescu, L.; Yakunin, S.; Nazarenko, O.; Dirin, D. N.; Kovalenko, M. V. Low-Cost Synthesis of Highly Luminescent Colloidal Lead Halide Perovskite Nanocrystals by Wet Ball Milling. *ACS Appl. Nano Mater.* **2018**, *1* (3), 1300–1308.
- (31) Tian, J.; Zysman-Colman, E.; Morrison, F. D. Compositional Variation in Hybrid Organic–Inorganic Lead Halide Perovskites: Kinetically versus Thermodynamically Controlled Synthesis. *Chem. Mater.* **2021**, *33* (10), 3650–3659.
- (32) Prochowicz, D.; Yadav, P.; Saliba, M.; Saski, M.; Zakeeruddin, S. M.; Lewiński, J.; Grätzel,

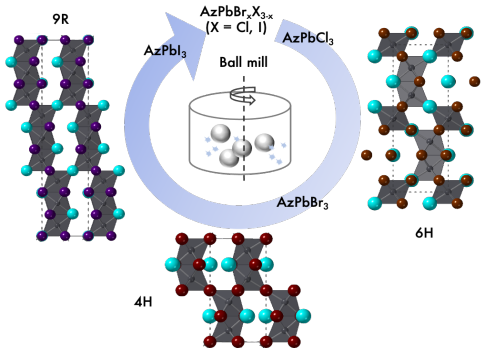
- M. Mechanosynthesis of Pure Phase Mixed-Cation MA_xPbI_{3-x} Hybrid Perovskites: Photovoltaic Performance and Electrochemical Properties. *Sustain. Energy Fuels* **2017**, *1* (4), 689–693.
- (33) Vidyasagar, C. C.; Muñoz Flores, B. M.; Jiménez Pérez, V. M. Recent Advances in Synthesis and Properties of Hybrid Halide Perovskites for Photovoltaics. *Nano-Micro Lett.* **2018**, *10* (4), 68.
- (34) Hong, Z.; Tan, D.; John, R. A.; Tay, Y. K. E.; Ho, Y. K. T.; Zhao, X.; Sum, T. C.; Mathews, N.; García, F.; Soo, H. Sen. Completely Solvent-Free Protocols to Access Phase-Pure, Metastable Metal Halide Perovskites and Functional Photodetectors from the Precursor Salts. *iScience* **2019**, *16* (0), 312–325.
- (35) Abdelhady, A. L.; Saidaminov, M. I.; Murali, B.; Adinolfi, V.; Voznyy, O.; Katsiev, K.; Alarousu, E.; Comin, R.; Dursun, I.; Sinatra, L.; et al. Heterovalent Dopant Incorporation for Bandgap and Type Engineering of Perovskite Crystals. *J. Phys. Chem. Lett.* **2016**, *7* (2), 295–301.
- (36) Zhang, Z.; Ren, L.; Yan, H.; Guo, S.; Wang, S.; Wang, M.; Jin, K. Bandgap Narrowing in Bi-Doped CH₃NH₃PbCl₃ Perovskite Single Crystals and Thin Films. *J. Phys. Chem. C* **2017**, *121* (32), 17436–17441.
- (37) Ng, M.; Halpert, J. E. Single Crystals of Mixed Br/Cl and Sn-Doped Formamidinium Lead Halide Perovskites *via* Inverse Temperature Crystallization. *RSC Adv.* **2020**, *10* (7), 3832–3836.
- (38) Kubicki, D. J.; Prochowicz, D.; Pinon, A.; Stevanato, G.; Hofstetter, A.; Zakeeruddin, S. M.; Grätzel, M.; Emsley, L. Doping and Phase Segregation in Mn²⁺- and Co²⁺-Doped Lead Halide Perovskites from ¹³³Cs and ¹H NMR Relaxation Enhancement. *J. Mater. Chem. A* **2019**, *7* (5), 2326–2333.
- (39) Arya, S.; Mahajan, P.; Gupta, R.; Srivastava, R.; Tailor, N. kumar; Satapathi, S.; Sumathi, R. R.; Datt, R.; Gupta, V. A Comprehensive Review on Synthesis and Applications of Single Crystal Perovskite Halides. *Prog. Solid State Chem.* **2020**, *60*, 100286.
- (40) Kieslich, G.; Sun, S.; Cheetham, A. K.; Cheetham, T.; Gregor, K.; Shijing, S.; Anthony, K.

C. Solid-State Principles Applied to Organic-Inorganic Perovskites: New Tricks for an Old Dog. *Chem. Sci.* **2014**, *5* (12), 4712–4715.

- (41) Shannon, R. D. Revised Effective Ionic Radii and Systematic Studies of Interatomic Distances in Halides and Chalcogenides. *Acta Crystallogr. Sect. A* **1976**, *32* (5), 751–767.
- (42) Panetta, R.; Righini, G.; Colapietro, M.; Barba, L.; Tedeschi, D.; Polimeni, A.; Ciccioli, A.; Latini, A. Azetidinium Lead Iodide: Synthesis, Structural and Physico-Chemical Characterization. *J. Mater. Chem. A* **2018**, *6* (21), 10135–10148.
- (43) Wang, W.; Su, J.; Zhang, L.; Lei, Y.; Wang, D.; Lu, D.; Bai, Y. Growth of Mixed-Halide Perovskite Single Crystals. *CrystEngComm* **2018**, *20* (12), 1635–1643.
- (44) Jesper Jacobsson, T.; Correa-Baena, J. P.; Pazoki, M.; Saliba, M.; Schenk, K.; Grätzel, M.; Hagfeldt, A. Exploration of the Compositional Space for Mixed Lead Halogen Perovskites for High Efficiency Solar Cells. *Energy Environ. Sci.* **2016**, *9* (5), 1706–1724.
- (45) Levchuk, I.; Osvet, A.; Tang, X.; Brandl, M.; Perea, J. D.; Hoegl, F.; Matt, G. J.; Hock, R.; Batentschuk, M.; Brabec, C. J. Brightly Luminescent and Color-Tunable Formamidinium Lead Halide Perovskite FAPbX₃ (X = Cl, Br, I) Colloidal Nanocrystals. *Nano Lett.* **2017**, *17* (5), 2765–2770.
- (46) A. C. Larson and R.B. V. Dreele. *Los Alamos National Laboratory Report LAUR*; 2004.
- (47) Holder, C. F.; Schaak, R. E. Tutorial on Powder X-Ray Diffraction for Characterizing Nanoscale Materials. *ACS Nano* **2019**, *13* (7), 7359–7365.
- (48) Mohd Yusoff, A. R. Bin; Gao, P.; Nazeeruddin, M. K. Recent Progress in Organohalide Lead Perovskites for Photovoltaic and Optoelectronic Applications. *Coord. Chem. Rev.* **2018**, *373*, 258–294.
- (49) Kumawat, N. K.; Dey, A.; Kumar, A.; Gopinathan, S. P.; Narasimhan, K. L.; Kabra, D. Band Gap Tuning of CH₃NH₃Pb(Br_{1-X}Cl_X)₃ Hybrid Perovskite for Blue Electroluminescence. *ACS Appl. Mater. Interfaces* **2015**, *7* (24), 13119–13124.
- (50) Park, B.; Philippe, B.; Jain, S. M.; Zhang, X.; Edvinsson, T.; Rensmo, H.; Zietz, B.; Boschloo, G. Chemical Engineering of Methylammonium Lead Iodide/Bromide

Perovskites: Tuning of Opto-Electronic Properties and Photovoltaic Performance. *J. Mater. Chem. A* **2015**, *3* (43), 21760–21771.

- (51) Wang, L.; Yuan, G. D.; Duan, R. F.; Huang, F.; Wei, T. B.; Liu, Z. Q.; Wang, J. X.; Li, J. M. Tunable Bandgap in Hybrid Perovskite $\text{CH}_3\text{NH}_3\text{Pb}(\text{Br}_{3-y}\text{X}_y)$ Single Crystals and Photodetector Applications. *AIP Adv.* **2016**, *6* (4), 045115.
- (52) Lee, S.; Levi, R. D.; Qu, W.; Lee, S. C.; Randall, C. A. Band-Gap Nonlinearity in Perovskite Structured Solid Solutions. *J. Appl. Phys.* **2010**, *107* (2), 1–6.
- (53) Chatterjee, S.; Payne, J.; Irvine, J. T. S.; Pal, A. J. Bandgap Bowing in a Zero-Dimensional Hybrid Halide Perovskite Derivative: Spin-Orbit Coupling: Versus Lattice Strain. *J. Mater. Chem. A* **2020**, *8* (8), 4416–4427.
- (54) Goyal, A.; McKechnie, S.; Pashov, D.; Tumas, W.; Schilfgaarde, M. Van; Stevanović, V. Origin of Pronounced Nonlinear Band Gap Behavior in Lead-Tin Hybrid Perovskite Alloys. *Chem. Mater.* **2018**, *30* (11), 3920–3928.
- (55) Hu, Z.; Lin, Z.; Su, J.; Zhang, J.; Chang, J.; Hao, Y. A Review on Energy Band-Gap Engineering for Perovskite Photovoltaics. *Sol. RRL* **2019**, *3* (12), 1–9.
- (56) Lehmann, F.; Franz, A.; Többens, D. M.; Levcenco, S.; Unold, T.; Taubert, A.; Schorr, S. The Phase Diagram of a Mixed Halide (Br, I) Hybrid Perovskite Obtained by Synchrotron X-Ray Diffraction. *RSC Adv.* **2019**, *9* (20), 11151–11159.



For Table of content only

Highly stable mixed halide perovskites $\text{AzPbBr}_{3-x}\text{X}_x$ ($\text{X} = \text{Cl}$ or I) were obtained by mechanosynthesis. A structural progression from 6H, 4H to 9R perovskite polytype with varying halide composition is observed. X-ray diffraction shows a linear variation in unit cell volume as a function of the average anion radius not only within the solid solution of each polytype but uniformly across all three polytypes. This is correlated with a linear tuning of the bandgap from 3.43 to 2.00 eV.